

3D Surface Shape Information from Fringe Projection Techniques

Pedro Barradas, pedronevesbarradas@gmail.com

Abstract—Obtaining 3D models of objects from imaging techniques, has become of increasing interest during the last few decades due to its potential in real world applications, leading to the appearance of technologies, such as, the interferometric synthetic aperture radar (InSAR), magnetic resonance imaging (MRI) and optical interferometry. In this work were studied the principles involved in geometric image formation of a camera and projector system and the Digital fringe projection interferometry method, in particular, a Four Step Phase shifting technique. A 3D scanner system was implemented, taking into account the camera and projector calibration, the study and the correction of photographic effects, namely, the vignetting and the nonlinearities in brightness due to hardware characteristics. A Bayesian Phase unwrapping algorithm was used to obtain the phase map of the objects subjected to 3D reconstruction, and a reference plane method was used to obtain the Phase to depth map conversion. Two objects of known dimensions were used to evaluate the mean squared error and the relative error of the phase to depth conversion. Furthermore, to delve deeper into the concepts learned, and to provide ground truth to the results produced by the experiments, was developed in Matlab a simulator of a digital light projection and acquisition system.

Index Terms—3D shape measurements, Digital fringe projection, Four Step Phase shifting technique, Phase unwrapping, Phase to depth conversion

I. INTRODUCTION

OPTICAL Optical profilometry is a non-contact interferometric-based method for characterizing surface topography, also known as surface texture. Interferometry is a measurement method that uses the phenomenon of interference of waves, usually electromagnetic, given the changes of displacement due to the wave's characteristics and the materials they interact with. In this thesis, we focus on the use of structured visible light waves, and fringe projection profilometry. By using at least two waves, an interference pattern can be formed by their superposition. These superposition interference patterns can either be obtained by projecting simultaneously the set of waves and acquiring the result, or projecting one wave at a time and computing the result using adequate mathematical models. Making use of this technique, fringe projection profilometry systems aim to solve the problem of measuring 3D shapes of surfaces in a wide range of applications, such as 3D face reconstruction for robust face recognition systems, cultural heritage and preservation, 3D shape of microelectomechanical systems and measurement of flatness of panels. This research work has the objective of implementing a projection profilometry demonstrator (comprised of a digital light projector and a camera) that performs 3D shape measurements based on the phase shifting technique for fringe projection. Is

also part of our goal to develop a simulation software in MATLAB to provide ground truth to the obtained results. Fringe projection techniques have evolved tremendously in the past decades with contributions in the design of the projected patterns, on equipment induced error evaluation, on development of new fringe analysis methods to extract phase distribution, improvement of existing fringe analysis methods, phase unwrapping algorithms, calibration techniques and applications. Fringe projection techniques are classified, depending on the method used for the measurement. For example, phase stepping profilometry (PSP), for phase shifting methods [17]–[21], Fourier transform profilometry (FTP), for methods based on the Fourier transform [22]–[24] and wavelet transform profilometry (WTP), for methods based on wavelet transform [25]–[27]. In this paper, we will begin to explain the basic steps of a fringe profilometry system, give some background in image formation, in particular, on the phase stepping profilometry method implemented, and go through each step explaining our solution. In section V we describe our simulation software. We proceed to present some simulation and real world results and finally we draw some conclusions and point some directions for future work.

II. FRINGE PROFILOMETRY STEPS

The measurement of shape through fringe projection techniques involves the basic steps depicted on the following flowchart: The first step involves the study of the hard-

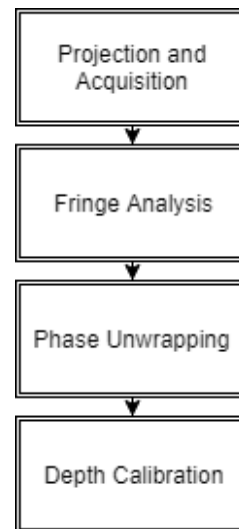


Fig. 1. Fringe profilometry steps.

ware used and correction of the photographic effects such

as vignetting and linearity in order to generate the fringes, the projection and the acquisition. The second step involves generating the interferogram from the acquired fringe images. The third step is obtaining the continuous phase distribution and finally the conversion of the unwrapped phase map to a depth map.

III. BACKGROUND

A. Geometric Image Formation

To define the location and orientation of the camera reference frame in relation to the world reference frame, the extrinsic parameters are required, and the intrinsic parameters to link the pixel coordinates of an image with their respective image points. The extrinsic parameters are defined as a set of geometric parameters that uniquely identify the transformation between the unknown camera reference frame and a known world reference frame. The most common format for doing so is to define a translation vector describing the relative position between the origin of each referential and an orthogonal rotation matrix that brings the corresponding axes of the two frames onto each other (see figure 2). The intrinsic parameters

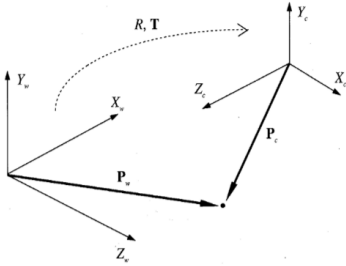


Fig. 2. The relation between the camera and the world coordinates. Adapted from [14].

define the optical, geometric, and digital characteristics of the viewing camera. For a pinhole camera there are needed:

- The perspective projection focal length, f .
- The transformation between the camera frame coordinates, (x, y) and the pixel coordinates (u, v) .
- The geometric distortion introduced by optics.

Let R be a rotation matrix (this is, $R^T R = I$, where I denotes the identity matrix of suitable size), defined as

$$R = \begin{bmatrix} r_{11} & r_{12} & r_{13} \\ r_{21} & r_{22} & r_{23} \\ r_{31} & r_{32} & r_{33} \end{bmatrix} \quad (1)$$

and, the translation vector be defined as,

$$T = [\delta X, \delta Y, \delta Z]^T. \quad (2)$$

Neglecting any geometric distortions we have:

$$x = -(u - o_x)s_x, \quad (3)$$

$$y = -(v - o_y)s_y, \quad (4)$$

where, o_x, o_y , are the image center coordinates in pixel, s_x, s_y the size of the pixel and u and v are the coordinates of an image point in pixel units. The image center coordinates,

the size of the pixel, and focal length are usually expressed in millimeters. Ignoring the radial distortion we have for intrinsic parameters o_x, o_y, s_x, s_y , and f . We can express the intrinsic transformation as,

$$M_{int} = \begin{bmatrix} -f & 0 & o_x \\ s_x & 0 & 0 \\ 0 & -f & o_y \\ 0 & 0 & 1 \end{bmatrix} \quad (5)$$

and, for the extrinsic transformation, we have

$$M_{ext} = \begin{bmatrix} r_{11} & r_{12} & r_{13} & -R_1^T T \\ r_{21} & r_{22} & r_{23} & -R_2^T T \\ r_{31} & r_{32} & r_{33} & -R_3^T T \end{bmatrix} \quad (6)$$

where, R_i corresponds to the i -th row of the matrix R . Finally, if we include a 1 as a fourth coordinate to the world point, so that a world point becomes $P_w = [X, Y, Z, 1]$, we obtain the linear Matrix equation of perspective projections:

$$[x_1, x_2, x_3]^T = M P_w^T. \quad (7)$$

where, $M = M_{int} M_{ext}$.

We now address the radial distortion. Herein we adopt the widespread used BrownConrady's [14] model. In this model, the radial distortion correction is achieved by applying two non-linear transformations to the image plane pixels. The first transformation takes the distortion introduced by the lens pixel coordinates and converts them into the undistorted pixel coordinates. Ignoring the tangential distortion correction, the transformations are defined as

$$P'_{u,v} = P_{u,v} (1 - a_{u,v} \|P\|_2^2) \quad (8)$$

$$P_{u,v} = \frac{P'_{u,v}}{1 - a_{u,v} \left\| \frac{P}{1 - a_{u,v} \|P\|_2^2} \right\|_2^2} \quad (9)$$

where u, v are the coordinates of an image point in pixel units, a_u and a_v are model parameters, P is a vector, and $P_{u,v}$ and $P'_{u,v}$ are the $uovv$ undistorted coordinates of an image point respectively. In the transformation expressions the coordinates are normalized to the domain $[-1, 1]$ in order to be consistent with any resolution. To obtain the normalized coordinates, we apply expression (10), (11) and to go back to the pixel coordinates we apply (12) and (13) [41].

$$P_u = \frac{2u - W}{W} \quad (10)$$

$$P_v = \frac{2v - H}{H} \quad (11)$$

$$u = \frac{(P_u + 1)W}{2} \quad (12)$$

$$v = \frac{(P_v + 1)H}{2} \quad (13)$$

The letters H and W represent the height and the width in pixel of the camera or the projector, in other words, its resolutions.

B. Phase stepping profilometry

The first algorithm of phase transition was introduced by James C. Wyant [28] making use of four phase shifts to calculate the interferogram. The basic idea of this technique can be understood by using four sinusoidal fringe patterns with shifts of θ radians between them. Let,

$$\begin{aligned} I_1(u, v) &= I_0 + I_{mod}(u, v)\cos(\phi(u, v)) \\ I_2(u, v) &= I_0 + I_{mod}(u, v)\cos(\phi(u, v) + \theta) \\ I_3(u, v) &= I_0 + I_{mod}(u, v)\cos(\phi(u, v) + 2\theta) \\ I_4(u, v) &= I_0 + I_{mod}(u, v)\cos(\phi(u, v) + 3\theta) \end{aligned}$$

be the mathematical model for the four captured fringe patterns where, $I_1(u, v)$, $I_2(u, v)$, $I_3(u, v)$, and $I_4(u, v)$ are the light intensities of four fringes, $I_0(u, v)$ is the DC component (background), $I_{mod}(u, v)$ is the modulation signal amplitude, $\phi(u, v)$ is the phase, and $\theta = \frac{\pi}{2}$ is a constant phase-shift. The wrapped phase information $\phi(u, v)$ can be retrieved from the intensities in the four fringe patterns using equation (14) [29]. Subsequently, it is necessary to unwrap the phase removing the discontinuity of the arctangent function at 2π by adding or subtracting multiples of 2π on the value of ϕ , as expressed by equation (15), where k is an integer representing a $\frac{\pi}{2}$ multiple. Solving this problem is known as *phase unwrapping* problem and this can be addressed in many ways as we will briefly explain in the next chapter.

$$\phi(u, v) = \arctan\left(\frac{I_4 - I_2}{I_1 - I_3}\right). \quad (14)$$

$$\phi_{unwrapped}(u, v) = \phi(u, v) + 2k\pi. \quad (15)$$

After obtaining the unwrapped phase, the real world three-dimensional coordinates can be obtained for example by calculating the difference between the measured phase $\phi(u, v)$ and the phase value from a reference plane. Figure 3 illustrates a simple case where,

$$\frac{Z}{L - Z} = \frac{d}{B}, \quad (16)$$

Finally, simplifying the relationship leads to,

$$Z \approx \frac{L}{B}d \propto \frac{L}{B}(\phi_1 - \phi_2) \quad (17)$$

where, ϕ_1 and ϕ_2 represent the unwrapped phases of the reference plane alone and the reference plane plus the object, respectively.

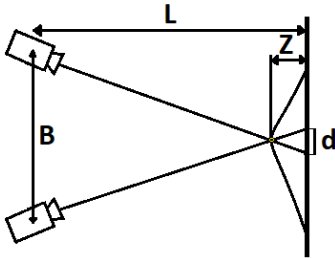


Fig. 3. Illustration of the geometry of the system, projector camera object reference plane.

IV. IMPLEMENTATION

In order to set up the real world experiment to achieve better results, we take on a few steps before generating the fringe patterns. In this section, we address these steps and describe how we implemented the 3D shape measurement processes.

A. Nonlinearity Correction

The system linearity with respect to brightness is a very important factor that should be taken into account. Without good linearity between pixel brightness of transmitted and received images, the phase data would be erroneous and the whole process results would be compromised. Our goal is to include the knowledge about the linearity of the system to generate good fringe patterns. In order to study the camera/projector setup in terms of this effect, we pre-calibrated the setup, and generated a sequence of projector resolution, grey scale (equal intensity of red green and blue) images with various intensities. In our case, a total of 255 images with digital levels ranging from 0 to 255 respectively in an 8 bit RGB image representation were used. A data set was obtained by projecting the generated grey scale images and acquiring them one by one. The acquired images are stored in memory with values of RGB for each image pixel in camera resolution. It would be possible to do a linearity study for every pixel of the captured images and obtain the correspondent linearity curves, although, assuming that the captured intensity of neighbouring pixels in certain location does not vary much (if hardware manufacture defects are absent), it is reasonable to focus our study only on some regions of the images. Our choice was to pick 9 square zones of 16 by 16 pixels, as depicted on Figure 4. For each of those zones we computed the mean

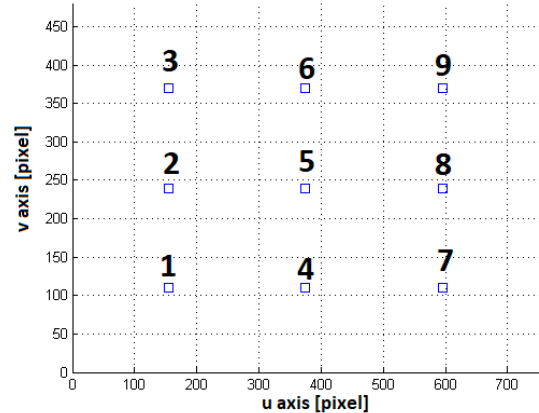


Fig. 4. Chosen locations of the 16 by 16 pixel squares for calibration of brightness linearity. Vertical and horizontal axis represent the coordinates in pixel.

value of the intensity of the captured images, and we plot it versus the intensity level of the grey scale projected images. Recall, that the captured data has RGB individual image data for each pixel, thus, for each grey scale image, we have to perform three separate linearity graphs for red, green and blue respectively. In summary, we obtained 3 graphs with 9 curves each, of the system linearity information in total

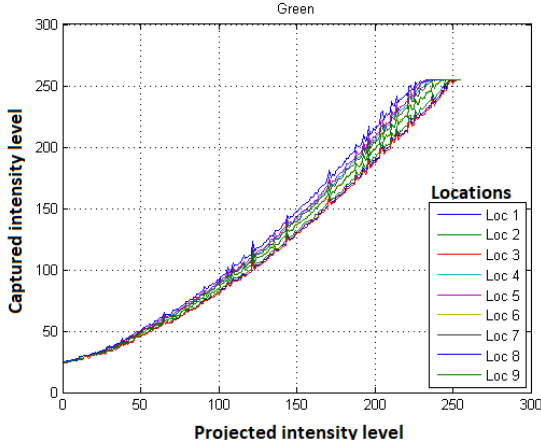


Fig. 5. Example of linearity curves for captured data. Vertical and horizontal axis represent the quantization levels for color intensity.

as depicted in Figure 5 for the green component. Finally, according to the data we can design the fringe patterns so that the dynamic intensity range is contained in the linear domain of our projector/camera system.

B. Vignetting

In order to calibrate the vignetting effect, we project a grey level image with mid range brightness onto a reference plane surface, and capture the result with the camera (the captured image must be completely covered by the projected image). Reading the captured image intensity value at each pixel and dividing it by the expected projected value we obtain the ratios for the vignetting mask. Note that, as in the case of the linearity study, the read data consists of values for red, green, and blue, and so three vignetting masks are obtained. Let, $I_{R_{red}}$ be the captured image red values for intensity. Taking into account that the generated grey image has the same RGB intensity we get for every pixel i, j :

$$V_{i,j} = \frac{I_{R_{i,j}}}{I_{P_{i,j}}}. \quad (18)$$

Where $V_{i,j}$ is an entry of the vignetting mask gain for the red color corresponding to pixel coordinates i, j . $I_{R_{i,j}}$, and $I_{P_{i,j}}$ are respectively the received and projected intensity values at i, j location. This vignetting mask is a matrix of the computed ratios ($V_{i,j}$). The vignetting calibration then consists in taking every image pixel value and dividing each red, green, and blue entries by its respective vignetting mask gain (see expression 19).

$$C_{i,j} = \frac{I_{i,j}}{V_{i,j}}. \quad (19)$$

Where $C_{i,j}$ represents the corrected value for the image pixel (i, j) . $C_{i,j}$ represents the corrected value for the image pixel (i, j) .

C. Pattern Generation

In phase shifting interferometry the most common fringe patterns consist of vertical constant phase lines with horizontal

sinusoidal variation of a specified period. Usually, this period can be controlled to achieve different levels of granularity of the final result. The precision in depth measurements is highly dependent on fringe frequency, because the $2k\pi$ jumps of phase unwrapping relate directly to wave length. The fringe patterns can be generated according to

$$I(u, v) = A \left[\frac{1 - \cos(\omega(u, v) + \phi)}{2} \right] + m. \quad (20)$$

In this equation $A = \frac{M-m}{255}$, where M and m represent the maximum and minimum values of brightness read from the linearity curves, so that the system remains working in the linear region. As an example, if $M = 200$ and $m = 50$ $A = \frac{150}{255}$ and $M - m = 150$ is the dynamic range of brightness of the pattern. From this equation, A reshapes the amplitude and m determines the minimum level for the brightness of the pattern. The angular frequency of horizontal variation $\omega(u, v)$ is given by equation (21), where W is the number of vertical lines of the image, f is the frequency of the fringe pattern and v is the vertical line coordinate. The value ϕ corresponds to the phase shift control variable that is changed in order to generate many different patterns.

$$\omega(u, v) = \omega(v) = v \frac{2f\pi}{W-1}. \quad (21)$$

D. Interferogram

The basic concept about phase-shifting interferometry lies in the study of the interference between a known reference signal, like the light emitted by a laser, with one reflected on the surface of an object. For the L -step phase-shifting interferometry, the complex-valued wave front at the sensor plane is given by

$$u_s = B_0 e^{j\phi_0} + A_r e^{-j\phi_{rs}}, \quad s = 1, \dots, L, \quad (22)$$

where, $B_0 e^{j\phi_0}$ and $A_r e^{-j\phi_{rs}}$ are the object and reference wave fronts respectively, ϕ_{rs} is a controllable phase shift and L defines the number of shifts. Assuming that the sensor takes measurements in a rectangular grid with N elements, let Y_s , $s = 1, \dots, L$, denote the L measured images and $Y_s(l)$, $l = 1, \dots, N$ the intensity of each of its N elements. It can be shown that $I_s(l) = |u_s|^2$ the intensity of the wavefront at the pixel l , is given by

$$I_s = B_0 e^2 + A_r^2 + 2B_0 A_r \cos(\phi_0 + \phi_{rs}). \quad (23)$$

Following the Poisson observations model,

$$p(Y_s[l] = k) = e^{-I_s[l]\chi} \frac{(I_s[l]\chi)^k}{k!}, \quad (24)$$

where, each element of the photo sensor is modelled as an independent random variable, $p(Y_s[l] = k)$, denotes the probability of a k number of photons hitting the photo sensor l , and χ is a scaling factor. Replacing the observations Y_s by $\frac{Y_s}{\chi}$ and taking into account the scaling factor, for example, due to different exposure time or sensor sensitivity, and taking the particular case of $L=4$, a total of four phase shifts taking

values in the set $\{0, \frac{\pi}{2}, \pi, \frac{3\pi}{2}\}$, the least squares formulation for the phase and the amplitude of the object is given by

$$(\tilde{\phi}_0, \tilde{B}_0) = \arg \min_{\phi_0, B_0} \sum_{s=1}^4 \left\| \frac{Y_s}{\chi} - B_0^2 + A_r^2 + 2B_0^2 A_r \cos(\phi_0 + \phi_{rs}) \right\|_2^2 \quad (25)$$

yielding the solution for the phase,

$$\phi_0 = \arctan\left(\frac{Y_4 - Y_2}{Y_1 - Y_3}\right). \quad (26)$$

This result is the so called interferogram. So, the process used to obtain the interferogram is to obtain 4 pictures of the same object with 4 different phase-shifted patterns and to compute for each pixel the value of ϕ_0 .

E. Phase unwrapping

Let, $W(\cdot)$ be a wrapper operator defined as

$$\begin{aligned} W : \mathbb{R} &\rightarrow [0, 2\pi[\\ \phi &\rightarrow \text{mod}(\phi + \pi, 2\pi) \end{aligned} \quad (27)$$

where $\text{mod}(\cdot)$ is the modulus after division by 2π . Notice that $W(\phi) = W(\phi + 2k\pi)$, where k is an interger. The inverse operation that yields ϕ from $\phi - 2\pi k$ constitutes the phase unwrapping problem. The variable ϕ is the absolute phase that, in our case, is directly linked to the deformation of the fringe pattern relatively to a reference plane, and is correlated with the depth of the object. Note that, the wrapper operator as well as its inverse can also be defined in a different interval of the same length, such as $[-\pi, \pi[$. Phase unwrapping is an ill-posed problem, this is, a certain wrapped phase value can lead, in theory, to an infinite number of solutions for the absolute phase value. Although this problem of phase unwrapping can pose difficulties in some cases, it can be solved given additional or a priori information up to a constant. The condition that simplifies the phase unwrapping problem is known as the Itoh condition [36], which ascertains that the phase difference between any pixel and its neighbouring pixels is less than π radians. This is equivalent to assume that the surface of the object is spatially smooth or piecewise smooth. The Itoh condition immediately provides a phase unwrapping method, which employs the use of a path following concept. The simplest method integrates the phase differences along a certain path between any pixel of unknown absolute phase to a pixel whose absolute phase is known. A problem with this algorithm, reported by Ghiglia et al. in [37], is that the discrete integration of the phase differences is not path independent. The closed loop integration of phase differences is always a multiple of 2π unless there are inconsistencies known as residues, and the sign of the residue is known as the charge of the residue. These residues cause the path following dependency, and there are many strategies to solve it. One of them is to connect the opposite charge residues with certain line paths that cannot be crossed over by any integration path of the regular path following methods. This strategy, known as Branch cutting. Other algorithms such as quality guided methods use different strategies to avoid residues. The path following algorithms are local methods in nature. Another

class of algorithms take a completely different concept and adopt a global perspective via optimization procedures that involve the image as a whole, such as L^p norm Algorithms, and Bayesian and parametric methods. In the context of phase unwrapping, we will be using the ‘‘PUMA’’ algorithm based on a Bayesian method implemented by Gonalo Matias and by Bioucas Dias [38].

F. Phase to depth conversion

The step after obtaining the unwrapped phase map is to convert this phase map to depth. There are two main approaches:

- Analytical approaches
- Experimental approaches

Analytical geometric methods tend to be more precise but often result in more complicated calculations and many that contribute to increase the complexity of the algorithm. On the other hand experimental methods assume simpler relations between the phase map and three-dimensional coordinates. One of our solutions is to determine the absolute coordinates of every image pixel in the world coordinate system, like in S.Z. Hang, D.R.Oyer and S.Yau at [40]. Another method, less sophisticated, makes use of a reference plane and the phase map is obtained relative to it. In other words, the height map is determined in relation to the plane. For this method, the fringe patterns are projected onto the reference plane, the interferogram is computed, and the phase unwrapping process is applied. Then the object is put in front of the plane and we repeat the same steps, obtaining two phase maps. Subtracting the plane phase map from the plane with the object, we get the relative phase map. Figure 3 depicts the setup arrangement. From the triangle similarity, we obtain equation (28) and the relation between the relative phase to the distance d on the reference plane is give by equation (29)

$$\frac{d}{Z} = \frac{B}{L} \quad (28)$$

$$\phi_z(u, v) = 2\pi f_0 d. \quad (29)$$

Thus, the relation between the object height and the phase map obtained is given by equation (30)

$$Z(u, v) = \frac{L}{2\pi f_0 B} \phi_z(u, v) \quad (30)$$

V. SIMULATION

In this section we will go through the steps involved in the development of our simulation software.

A. Object definition

In simulation, we use a cube as the default object. To define a cube, a list of the coordinates of its vertices is all the information needed. Working with the camera reference frame as the origin of the world coordinates, we define an object’s orientation and location. In our simulation, the objects used are simple right angle solids, where a set of three-dimensional coordinates defines the object’s vertices. To express the orientation of the object, that is, its rotation around the world three dimensional axes, we define the Euler angles α , β and γ , and

use them to compute the rotation matrix. This is achieved by the same method employed previously, where we multiplied the matrices (31), (32), and (33). With the rotation matrix and the relative position vector, we obtain the transformation of coordinates (6) that defines the object's vertex coordinates in the world reference frame. The algorithm would still work with any rectangular solid, and it has conditions to be extended to work with any convex object, but for our purpose of understanding the basics of the physics involved in the fringe projection and acquisition problem we decided that working with simple shapes was enough.

B. Geometric image formation

According to the geometric image formation models described in the section III-A, in order to define the relative pose between camera and projector it is necessary a translation vector (2) and a rotation matrix (1). Defining these parameters is one of the first steps in our algorithm. We define the projector rotation matrix and translation vector, such that, the projector is facing directly the object's center. In our implementation, it was set such that the object would never have negative z coordinate values. We start by determining the direction of the z axis (equation (34)), where C_{obj} and C_{proj} are the vector coordinates of the centroid of the object of and the projector position in the world reference frame coordinates, respectively. (Note: u_z is a unit vector). The x axis direction is an orthonormal vector with no component in the y direction and is determined according to equations (35), (36), and (37), where the indices represent the i -th component of the u vectors and $u_{x,3}$ has the same sign of $u_{x,1}$.

$$R_\alpha = \begin{bmatrix} 1 & 0 & 0 \\ 0 & \cos \alpha & -\sin \alpha \\ 0 & \sin \alpha & \cos \alpha \end{bmatrix} \quad (31)$$

$$R_\beta = \begin{bmatrix} \cos \beta & 0 & \sin \beta \\ 0 & 1 & 0 \\ -\sin \beta & 0 & \cos \beta \end{bmatrix} \quad (32)$$

$$R_\gamma = \begin{bmatrix} \cos \gamma & -\sin \gamma & 0 \\ \sin \gamma & \cos \gamma & 0 \\ 0 & 0 & 1 \end{bmatrix} \quad (33)$$

$$u_z = \frac{C_{obj} - C_{proj}}{\|C_{obj} - C_{proj}\|_2} \quad (34)$$

$$u_{x,1} = \sqrt{\frac{u_{z,3}^2}{u_{z,1}^2 + u_{z,3}^2}} \quad (35)$$

$$u_{x,2} = 0; \quad (36)$$

$$u_{x,3} = \pm \sqrt{1 - \frac{u_{z,3}^2}{u_{z,1}^2 + u_{z,3}^2}}; \quad (37)$$

$$u_y = -u_x \times u_z \quad (38)$$

Finally, the y axis direction of the projector reference frame is determined by the negative of the cross product of the z and x axis unit vectors (38). Then, we define the camera and projector's resolutions, focal distance, pixel size, and compute

their respective pixel to world coordinate transformation matrices expressed by equation (7). Finally, to account for the lens distortion, we define the radial distortion parameters for both the projector and the camera with equations (8) and (9).

C. Modeling lens radial distortion

In order to determine the captured image, we systematically calculate the trajectory of the light rays, reflected on the object surface, that go through the camera lenses and hit the light sensor array. Light rays travel in straight lines, but we must take into account the radial distortion employed by the optical lenses of both the projector and the camera that, in turn, cause deviations from their original propagation directions. To do so, we simply use the determined a_u and a_v parameters representing, respectively, the vertical and horizontal distortion factors that are characteristic of the lenses, to compute the nonlinear pixel coordinates transformations referred in section III-A. We may refer to the transformation of distorted coordinates into undistorted coordinates as the direct transformation (8), and in contrast, refer as the inverse transformation (9) to the transformation that works the opposite way.

D. Simulator Fluxogram

In Figure we present a flowchart with the most important steps performed by the algorithm.

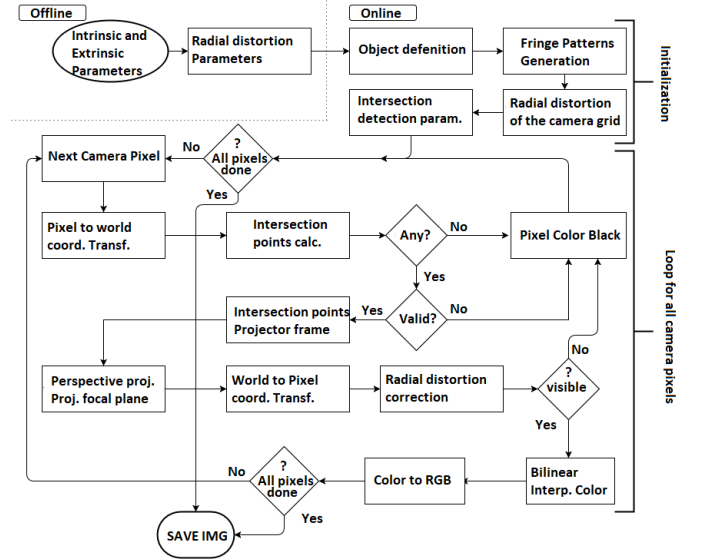


Fig. 6. Simulator Fluxogram.

VI. RESULTS

In this section we present some of the results obtained on our experiments.

A. Simulation

1) *Cube*: In table VI-A are listed the simulation parameters. Figures 7 and 8 represent the image from the simulator and the interferogram respectively. In Figure 9 depicts the unwrapped phase obtained from PUMA. Given the spatial frequency of

Simulation Parameters	Values
Center world = Camera position	$[0, 0, 0]$ [m]
Projector position	$[0.2, 0, 0]$ [m]
Fringe patterns spatial frequency	80 [cycles/resolution width]
Projecto and camera Resolution	1280x720 [pixel]
Pixel size	6 [μm]
CCD horizontal center	640 [pixel]
CCD vertical center	360 [pixel]
Focal Length	2.7[mm]
skew(s)	0
horizontal radial distortion (α_u)	0
vertical radial distortion (α_v)	0
Edges length	0.3 [m]
Euler rotation angles [α β γ]	$[0.2$ 0.5 $0.5]$ [rad]
Center	$[0, 0, 1.45]$ [m]

TABLE I
SIMULATION PARAMETERS.

the fringe patterns on the reference plane and the geometry of the setup, we can determine a constant of conversion between phase and depth, obtaining the height of each pixel relative to the plane according to equation (30). The result is depicted in Figure 10 and can be compared to Figure 11, where it is shown the expected values extracted directly from the simulator, resulting in a mean squared error of $2.6 * 10^{-3}$ [m].

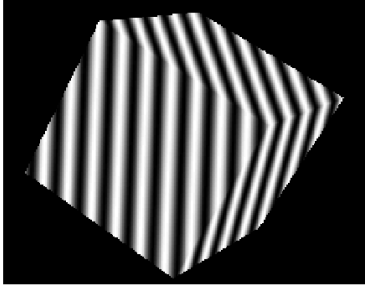


Fig. 7. Projection of the zero phase fringe pattern on the cube.

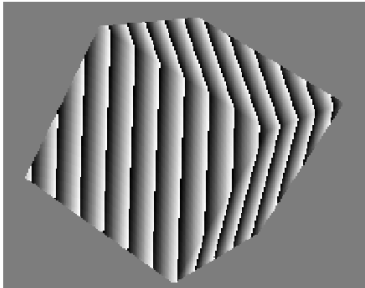


Fig. 8. Interferogram of the cube.

2) *Noisy Cube*: We repeated the experiment for noisy data. The added Gaussian noise has zero-mean and $\sigma^2 = 0.1$. In

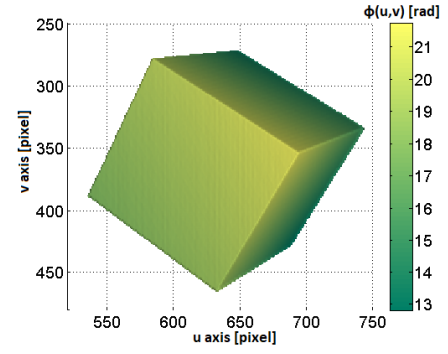


Fig. 9. Unwrapped phase of the cube.

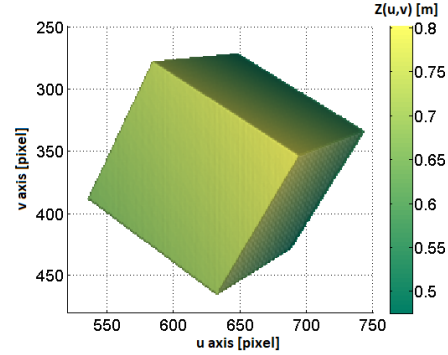


Fig. 10. Cube depth map.

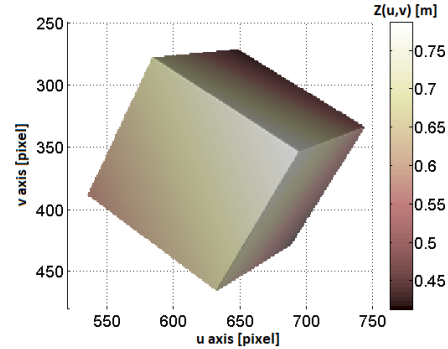


Fig. 11. Height Map prediction obtained from the simulator.

Figure 12 is depicted the noisy acquisition the cube, and in Figure 13 its unwrapped phase map.

In the results it is clear that the introduced noise, highly affected the smoothness of the cube's surface. This is a consequence of the noise sensitivity of the interferogram computation step.

B. Real World

On our setup we used the LED PG65U [44] projector from LG, the UI-1220LE iDS camera [43], the FUJINON YV5x2.7R4B-2 lens [42] and a 91.8 by 71.4 [cm] calibration checkerboard.

1) *Chico*: We calibrated the system camera/projector to obtain the intrinsic and extrinsic parameters. The calibration of the camera had approximately 0.6 [pixel] reprojection error,

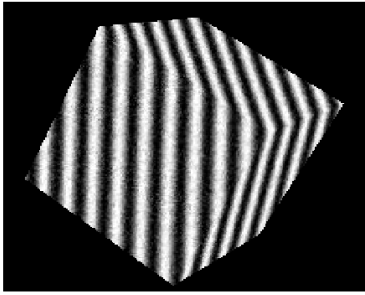


Fig. 12. Noisy acquisition of the cube.

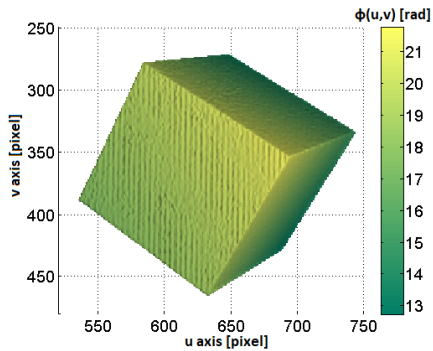


Fig. 13. Unwrapped phase of the noisy cube.

the projector reprojection error was approximately $0.9 [pixel]$, and the stereo calibration error for both the projector and the camera had a reprojection error of $0.8 [pixel]$ approximately. From the linearity study the brightness levels of the fringe patterns were set to the range 80 to 244 in a 8 bit representation and using the method described in section IV-B we obtained the vignetting correction mask depicted in figure 14. We

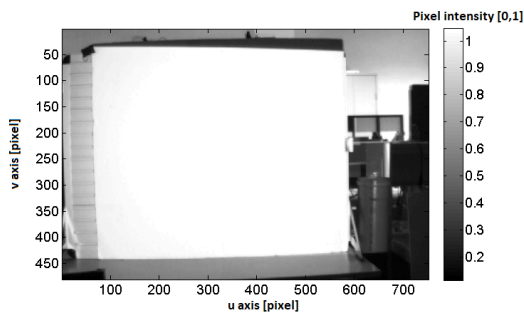


Fig. 14. Calibration parameters.

projected and captured images for the four fringe patterns. One example is depicted in Figure 15. Then, we corrected the vignetting effect by applying the correction mask to the four captured images. An example of the resultant vignetting corrected image is shown in Figure 16. Then, we computed the interferogram represented in Figure 17, and obtained the unwrapped phase. We repeat this process to the reference plane. Then, we subtract the unwrapped phase of the reference plane from the unwrapped phase map of “Chico+ref. plane”,

and we obtain the final result. To conclude, we applied a mask to remove the data of non-interest and obtained the unwrapped phase map depicted in figures 18 and 19.

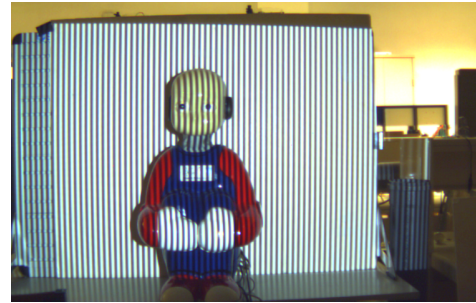


Fig. 15. Chico with fringe pattern.

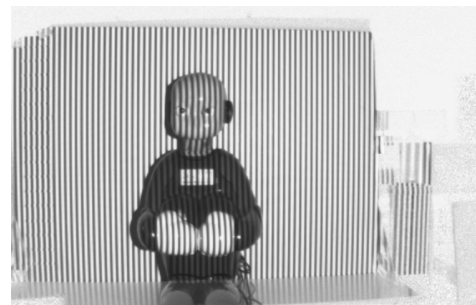


Fig. 16. Vignetting corrected Chico.

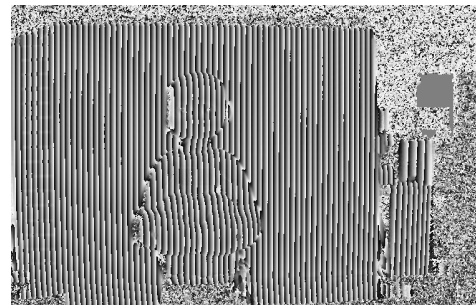


Fig. 17. Interferogram.

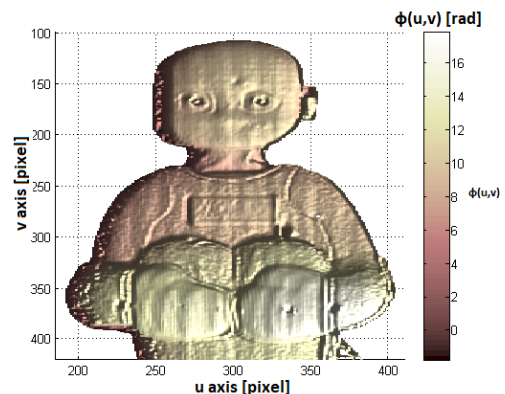


Fig. 18. Chico unwrapping front view.

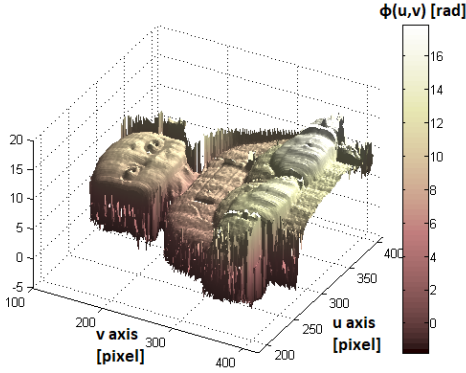


Fig. 19. Chico unwrapping side view.

C. Phase to depth calibration

In contrast to the simulation case where we possess the information about the depth map of the reconstructed object for each of the camera captured pixels, in the real experiment scenario, this is not the case. However, we can still try to obtain a phase to depth map. To obtain this phase to depth map we used two smaller planes of known dimensions. From the phase map, we averaged the unwrapped phase of the planes relative to the reference plane as shown in Figure 20. The average



Fig. 20. Areas used to average the unwrapped phase for planes 1 and 1+2.

value for difference of phase between the reference plane and plane 1 was $0.8149[rad]$ and for plane 2 was $1.6140[rad]$. Both planes have depth equal to $19 \pm 1[mm]$. Using plane 1 to calibrate the phase to depth conversion, we used expression

$$\psi = \frac{d}{\phi(u, v)} = \frac{19}{0.8149} = 23.3157 [mm/rad]. \quad (39)$$

Using this value to determine the plane 2 depth we get,

$$P^{1+2} = \phi(u, v) * \psi = 1.6140 * 23.3157 = 37.63 [mm], \quad (40)$$

where P^{1+2} is the depth of the superposition of planes 1+2. The measured depth of P^{1+2} is $38 \pm 1 [mm]$, which translates in root mean squared error of $0.37 [mm]$ and relative error of $\frac{0.37}{38} = 0.97\%$.

VII. CONCLUSIONS

The results obtained were quite satisfactory and proved that, even with off-the-shelf hardware, it is possible to obtain fairly accurate 3D reconstructions of objects using the method

explored in this thesis. Although we presented the results above without delving much into the details of the calculations that were made on our Matlab scripts, we want to point out a few important aspects. The first important aspect is the nature of the phase unwrapping algorithms. Phase unwrapping algorithms produce absolute phase results within a specific range of values uncertain up to a multiple of $2\pi k$, this is, the phase unwrapping results, $\phi_z(u, v)$, are often shifted, depending on the unwrapping algorithm, by a multiple of $2\pi k$. This implies that, for example, in the expression (30), $\phi_z(u, v)$ is actually determined up to a factor of $2\pi k$, that is, $\phi_z(u, v)$ is actually $\phi_z(u, v) + 2\pi k$. This result implies that, even if we use the same unwrapping algorithm and different quality maps, we most likely will get results shifted by a certain phase value. To solve this problem one can use a pixel from the reference plane contained in the quality map defined regions of both acquisitions to compute the phase shift difference. For example, if in the first acquisition one gets $\phi_1(100, 100) = 45 [rad]$ for the unwrapped phase and $\phi_2(100, 100) = 55[rad]$ for the second, one can correct the unwrapped phase map by adding or subtracting $10 [rad]$ to it so that the phase at the point $(u, v) = (100, 100)$ matches. Another important factor is the focus of the camera and the projector. Making sure the system is well focused can be evaluated from the calibration error. Lower calibration errors are important indicators for the overall quality of the reconstructions. At last, this type of phase unwrapping method is highly dependent of the roughness of the surfaces of the objects as well as the reflection factors of its surfaces. This is explained due to the fact that the phase determination is highly dependent on the light intensity detected by the camera sensor, and so it is expected that any light reflection perturbances or background illumination noise can influence the 3D shape determination and produce mistakes. In our real case experiments we had some background illumination issues and in the simulation we clearly can conclude in the noisy acquisition case that it changes the surface shape. Although in some cases it might not have an impact, for others it can constitute a problem depending on the precision required by the application.

A. Achievements

In this dissertation research, the following contributions were made:

(1) **A simulator of a projection and acquisition system comprised of a digital light projector and a camera.** The simulator is capable of generating the predicted acquisition of any image projected on top of a right angle plane faces object. It can work with different resolutions and intrinsic parameters for both the projector and the camera. It simulates noisy acquisition and radial distortion of the lenses.

(2) **A 3D shape measurement system based on optical interferometry, in particular a four phase shifting technique was implemented.** The systems extrinsic and intrinsic parameters were calibrated using a very accurate software developed by Daniel Moreno and Gabriel Taubin [34]. Furthermore, the nonlinearity working zones were determined and made sure

to be cut off, and finally the vignetting effect of the projector was taken into account and corrected.

B. Future Work

In this research, we successfully developed a simulation program and 3D surface scanner based on the phase shifting projection technique. However, there are many issues to be studied and explored. With respect to each of the developed components of this work we summarize some of the aspects that can be developed in the future or improved. Improving the simulator:

- Make the simulator work with different types of objects not only right angle plane face surface solids;
- Implement the code in another language faster than Matlab for faster performance.

Improving the real world experiments:

- Implement a shadow detection and removal technique to improve the quality map for the PUMA algorithm;
- Reduce the noise sensitivity issues of the interferogram computation, which generate results highly sensitive to noise of the acquisitions. For example, by introducing some kind of filtering like the one proposed by V. Katkovnik and J. Bioucas-Dias in [29].
- Test the limitations of the fringe projection technique to different surface roughness, and large phase discontinuities, this is, larger than π .
- Use other fringe interferometry techniques. For example, methods that make use of fringes with different frequencies simultaneously.

REFERENCES

- [1] Z. J. Geng. Rainbow three-dimensional camera: new concept of high-speed three-dimensional vision systems. *Optical Engineering*, 35(2):376–383, 1996.
- [2] Z. Geng. Color ranging method for high speed low-cost three dimensional surface profile measurement, Oct. 7 1997. US Patent 5,675,407.
- [3] D. J. Bone, H.-A. Bachor, and R. J. Sandeman. Fringe-pattern analysis using a 2-D fourier transform. *Appl. Opt.*, 25(10):1653–1660, May 1986.
- [4] Z. Geng. High speed three dimensional imaging method. U.S. patent 6,147,760, November 2000.
- [5] J. Geng. 3D surface profile imaging method and apparatus using single spectral light condition. U.S. patent 6,556,706, April 2003a.
- [6] J. Geng. Three-dimensional dental imaging method and apparatus having a reflective member. U.S. patent 6,594,539, July 2003b.
- [7] J. Geng. High speed laser three-dimensional imager. U.S. patent 6,660,168 B1, July 2003c.
- [8] J. Geng. Method and apparatus for 3D imaging using light pattern having multiple sub-patterns. U.S. patent 6,700,669, March 2004.
- [9] C. L. Heike, K. Upson, E. Stuhang, and S. M. Weinberg. 3D digital stereophotogrammetry: a practical guide to facial image acquisition. *Head & Face Medicine*, 6(1):18, Jul 2010.
- [10] K. Sato and S. Inokuchi. Range-imaging system utilizing nematic liquid crystal mask. Proceedings of International Conference on Computer Vision (IEEE Computer Society Press, 1987), pp. 657661.
- [11] K. Y. I. Ishii and K. Doi. High-speed 3D image acquisition using coded structured light projection. IEEE/RSJ International Conference on Intelligent Robots and Systems, 2007. IROS 2007 (IEEE, 2007), pp. 925930.
- [12] R. J. Valkenburg and A. M. McIvor. Accurate 3D measurement using a structured light system. *Image Vision Comput.* 16(2), 99110, 1998.
- [13] J. L. Posdamer and M. D. Altschuler. Surface measurement by space-encoded projected beam systems. *Comput. Graph. Image Processing* 18(1), 117, 1982.
- [14] E. Trucco and A. Verri. *Introductory Techniques for 3-D Computer Vision*, pages 28–40. 1996.
- [15] P. Bourke. Lens correction and distortion. <http://paulbourke.net/miscellaneous/lenscorrection/>, April 2002.
- [16] S. H. Rowe and W. T. Welford. Surface topography of non-optical surfaces by projected interference fringes. 216:786–787, 11 1967.
- [17] V. Srinivasan, H. C. Liu, and M. Halioua. Automated phase-measuring profilometry of 3-D diffuse objects. *Appl. Opt.*, 23(18):3105–3108, Sep 1984.
- [18] M. Chang and D.-S. Wan. On-line automated phase-measuring profilometry. *Optics and Lasers in Engineering*, 15(2):127 – 139, 1991.
- [19] X.-Y. Su, W.-S. Zhou, G. von Bally, and D. Vukicevic. Automated phase-measuring profilometry using defocused projection of a ronchi grating. *Optics Communications*, 94(6):561 – 573, 1992.
- [20] X.-Y. Su, G. von Bally, and D. Vukicevic. Phase-stepping grating profilometry: utilization of intensity modulation analysis in complex objects evaluation. *Optics Communications*, 98(1):141 – 150, 1993.
- [21] X. F. Meng, L. Z. C. X. Peng, A. M. Li, J. P. Guo, and Y. R. Wang. Wavefront reconstruction and three-dimensional shape measurement by two-step dc-term-suppressed phase-shifted intensities. *Opt. Lett.* 34, 2009.
- [22] X. Su and W. Chen. Fourier transform profilometry:: a review. *Optics and Lasers in Engineering*, 35(5):263 – 284, 2001.
- [23] F. Berryman, P. Pynsent, and J. Cubillo. The effect of windowing in Fourier transform profilometry applied to noise images. *Opt. Laser Eng.* 41, 2004.
- [24] M. Dai and Y. Wang. Fringe extrapolation technique based on fourier transform for interferogram analysis. *Opt. Lett.*, 34(7):956–958, Apr 2009.
- [25] A. Dursun, S. zder, and F. N. Ecevit. Continuous wavelet transform analysis of projected fringe patterns. *Measurement Science and Technology*, 15(9):1768, 2004.
- [26] J. Zhong and J. Weng. Spatial carrier-fringe pattern analysis by means of wavelet transform: wavelet transform profilometry. *Appl. Opt.*, 43 (26):4993–4998, Sep 2004.
- [27] M. A. Gdeisat, D. R. Burton, and M. J. Lalor. Spatial carrier fringe pattern demodulation by use of a two-dimensional continuous wavelet transform. *Appl. Opt.*, 45(34):8722–8732, Dec 2006.
- [28] Y.-Y. Cheng and J. C. Wyant. Multiple-wavelength phase-shifting interferometry. *Appl. Opt.*, 24(6):804–807, Mar 1985.
- [29] V. Katkovnik and J. Bioucas-Dias. Wavefront reconstruction in phase-shifting interferometry via sparse coding of amplitude and absolute phase. *J. Opt. Soc. Am. A*, 31(8):1801–1810, Aug 2014.
- [30] M. Takeda, H. Ina, and S. Kobayashi. Fourier-transform method of fringe-pattern analysis for computer-based topography and interferometry. *J. Opt. Soc. Am.*, 72(1):156–160, Jan 1982.
- [31] S. R. Bone D.J., Bachor H.A. Fringe-pattern analysis using a 2-d fourier transform. *Applied Optics*, May 1986.
- [32] D. R. Burton and M. J. Lalor. Multichannel fourier fringe analysis as an aid to automatic phase unwrapping. *Appl. Opt.*, 33(14):2939–2948, May 1994.
- [33] O. A. Skydan, M. J. Lalor, and D. R. Burton. Technique for phase measurement and surface reconstruction by use of colored structured light. *Appl. Opt.*, 41(29):6104–6117, Oct 2002.
- [34] D. Moreno and G. Taubin. Simple, accurate, and robust projector-camera calibration. In *2012 Second International Conference on 3D Imaging, Modeling, Processing, Visualization Transmission*, pages 464–471, Oct 2012.
- [35] S. Starczewski. Canon ef 50 mm f/1.2l usm lens review. <http://www.lenstip.com>, 2010.
- [36] K. Itoh. Analysis of the phase unwrapping algorithm. *Appl. Opt.*, 21 (14):2470–2470, Jul 1982.
- [37] D. C. Ghiglia, G. A. Mastin, and L. A. Romero. Cellular-automata method for phase unwrapping. *J. Opt. Soc. Am. A*, 4(1):267–280, Jan 1987.
- [38] J. M. Bioucas-Dias and G. Valadão. *Phase Unwrapping via Graph Cuts*, pages 360–367. Springer Berlin Heidelberg, Berlin, Heidelberg, 2005.
- [39] D. Ghiglia and M. Pritt. Two-dimensional phase unwrapping: theory, algorithms, and software. Wiley-Interscience, 1998.
- [40] S. Zhang, D. Royer, and S.-T. Yau. Gpu-assisted high-resolution, real-time 3-D shape measurement. *Opt. Express*, 14(20):9120–9129, Oct 2006.
- [41] Paul Bourke, *Lens Correction and Distortion*, <http://paulbourke.net/miscellaneous/lenscorrection/>, April,2002
- [42] http://www.fujifilm.com/products/optical_devices/pdf/cctv/security/varifocal/yv5x27r4b-sa2_e.pdf
- [43] <https://en.ids-imaging.com/store/ui-1220le.html>
- [44] <http://www.lg.com/us/home-video/lg-PG65U-portable-led-projector>